

# communications materials

ARTICLE



<https://doi.org/10.1038/s43246-021-00170-x>

OPEN

## Corner states in a second-order mechanical topological insulator

Chun-Wei Chen<sup>1,4</sup>, Rajesh Chaunsali<sup>2,4</sup>, Johan Christensen<sup>3</sup>, Georgios Theocharis<sup>2</sup> & Jinkyu Yang<sup>1✉</sup>

Demonstration of topological boundary modes in elastic systems has attracted a great deal of attention over the past few years due to its unique protection characteristic. Recently, second-order topological insulators have been proposed in manipulating the topologically protected localized states emerging only at corners. Here, we numerically and experimentally study corner states in a two-dimensional phononic crystal, namely a continuous elastic plate with embedded bolts in a hexagonal pattern. We create interfacial corners by adjoining trivial and non-trivial topological configurations. Due to the rich interaction between the bolts and the continuous elastic plate, we find a variety of corner states of and devoid of topological origin. Strikingly, some of the corner states are not only highly-localized but also tunable. Taking advantage of this property, we experimentally demonstrate asymmetric corner localization in a Z-shaped domain wall. This finding could create interest in exploration of tunable corner states for the use of advanced control of wave localization.

<sup>1</sup>Aeronautics and Astronautics, University of Washington, Seattle, WA, USA. <sup>2</sup>LAUM, CNRS-UMR 6613, Le Mans Université, Le Mans, France. <sup>3</sup>Department of Physics, Universidad Carlos III de Madrid, Leganès, Madrid, Spain. <sup>4</sup>These authors contributed equally: Chun-Wei Chen, Rajesh Chaunsali.  
✉email: [jkyang@aa.washington.edu](mailto:jkyang@aa.washington.edu)

**T**opological insulators provide researchers with efficient ways to tailor and control the energy flow. These topologically non-trivial phases have drawn growing attention, since the immunity to back-scattering—the key feature of topological protection—can help overcome defects and sharp bends during energy transfer. Realization of these topological boundary states has been demonstrated in classical systems, such as acoustics and mechanics, through mimicking the quantum Hall effect<sup>1,2</sup>, the quantum spin Hall effect<sup>3,4</sup>, or the quantum valley Hall effect<sup>5–9</sup>. Recently, higher-order topological insulators with multiple moments have been predicted theoretically<sup>10–12</sup>, and parallel experimental works of the second-order topological quadrupole insulators have been demonstrated in mechanics<sup>13</sup>, microwave circuits<sup>14</sup>, electrical circuits<sup>15</sup>, photonics<sup>16</sup>, and acoustics<sup>17</sup>.

To create a topological quadrupole insulator, negative hopping parameter is a requisite ingredient. In practice, however, the negative coupling needs much effort to design. Therefore, another way based on bulk dipole moments has been proposed to form a second-order topological insulator. By leveraging the crystalline symmetry, “filling anomaly” explains the existence of in-gap corner states in these insulators<sup>18</sup>. The corner states of such second-order topological crystalline insulators with vanishing quadrupole moment have been studied primarily in square<sup>19–26</sup> and Kagome lattices<sup>27–31</sup>. Recent studies in photonics<sup>32,33</sup> have shown that hexagonal lattices can also support corner modes with interesting properties, but their mechanical analog has been limited to discrete mechanical structures which lack the engineering potential and practicality<sup>34</sup>.

In this work, we propose a bolted plate structure as a continuous platform of a second-order topological insulator. The plate is decorated with bolts, which act as resonators, arranged in  $C_6$ -symmetric hexagonal lattice. For the topological characterization, we approximate our system with a thin plate attached with lumped-masses<sup>35</sup>. Then, the topological indices are determined based on the rotational symmetries of eigenmodes at the high-symmetry points in the Brillouin zone. By joining two topologically-distinct configurations, we report the generation of two different types of corner modes: one with topological origin and the other without it. Interestingly, we find that the one without topological origin exhibits tunability when adjacent domains are interchanged. By leveraging these characteristics, we experimentally demonstrate a one-way corner localization of mechanical waves in a Z-shaped domain wall. This asymmetric wave localization mechanism can be used for advanced control of energy flow.

## Results and discussion

**System and unit-cell dispersion.** In Fig. 1a, steel bolts are mounted hexagonally in an aluminum plate. See Fig. 1b for the graphical illustration of the unit cell. The lattice constant is  $a = 45$  mm.  $R$  is the circumferential radius of six bolts, which is a tuning parameter of creating the trivial and non-trivial band gap. The enlarged unit cell in Fig. 1c shows that as  $R$  increases, the six bolts gradually expand until reaching the limit of the unit cell’s boundary as represented in yellow; whereas, as the  $R$  decreases, the six bolts gradually merge into the center as indicated in red. The band structure of  $R = 1.0a/3$ ,  $R = 0.8a/3$ , and  $R = 1.1a/3$  are shown in Fig. 1d–f, respectively, based on finite element analysis (FEA, see “Methods” for more details). The color bar quantifies the dominance of plate displacement in out-of-plane ( $z$ ) direction, which is defined as  $\Pi_z = \frac{\int_V |w|^2 dV}{\int_V (|u|^2 + |v|^2 + |w|^2) dV}$ , where  $V$  is the volume of the plate of a unit cell and  $u$ ,  $v$ , and  $w$  are the displacement components in  $x$ ,  $y$ , and  $z$  axes. When  $\Pi_z = 1$ , it means

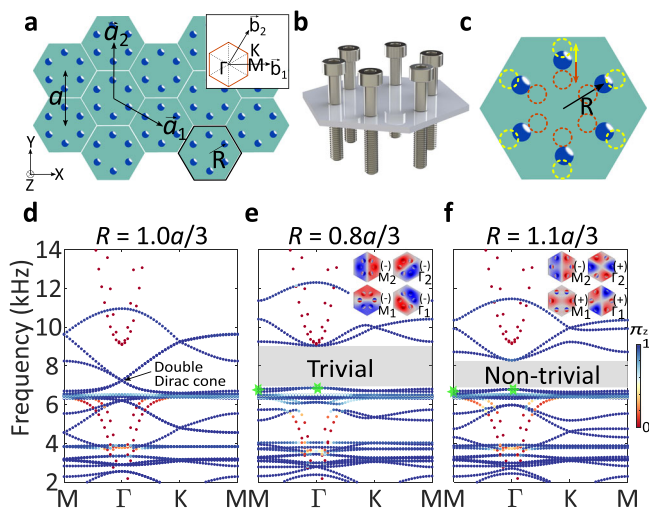


**Fig. 1 Unitcell and band structures.** **a** Continuous plate structure with hexagonally arranged bolts (blue dots). The translation vectors  $\vec{a}_1$  and  $\vec{a}_2$  and the corresponding reciprocal vectors  $\vec{b}_1$  and  $\vec{b}_2$  in the first Brillouin zone (inset). **b** A graphical illustration of the unit cell. **c** An enlarged plot of the unit cell with expanded ( $R > a/3$ , yellow) and shrunk ( $R < a/3$ , red) arrangements of the mounted bolts. **d**  $R = a/3$  case, which is exactly the honeycomb lattice with a double Dirac cone at the  $\Gamma$  point. Colorbar represents the level of the out-of-plane motion. **e**  $R = 0.8a/3$  case, which leads to the emergence of a trivial band gap represented in gray rectangle. Inset shows the four corresponding eigenmodes extracted from the marked green stars at the  $M$  and  $\Gamma$  points. **f**  $R = 1.1a/3$  case with a non-trivial band gap.

that the eigenmode is completely dominated by the out-of-plane motion; whereas, when  $\Pi_z = 0$ , the eigenmode is entirely dominated by the in-plane motion. From Fig. 1d, we see that there is a double Dirac cone at the  $\Gamma$  point at 7.27 kHz due to the zone-folding<sup>36</sup>. Once the radius  $R = a/3$  is no longer maintained, the double Dirac point opens and creates a band gap (Fig. 1e, f).

**Topological characterization.** We can perform the topological characterization of the band gaps based on the pseudospins of eigenmodes at the  $\Gamma$  point<sup>36,37</sup>. This analog of the quantum spin-Hall effect helps us predict the existence of chiral edge states at the interface between two domains made of shrunk ( $R < a/3$ ) and expanded ( $R > a/3$ ) unit cells. In the present study, however, we are interested in the corner states, and therefore, we characterize the band gaps based on quadrupole<sup>38</sup> or rotation invariants<sup>18,32,39</sup>. These rely on the parity (the eigenvalue of  $\pi$  rotation over the  $z$  axis) of eigenmodes at the  $\Gamma$  and  $M$  points of the Brillouin zone for every band below the band gap. In the insets of Fig. 1e, f, we plot eigenmodes for the first two bands immediately below the band gap at the  $\Gamma$  and  $M$  points (light green stars) and calculate their parity. For the shrunk configuration, the two bands have  $-1$  parity at the  $\Gamma$  and  $M$  points. However, for the expanded configuration, the two bands have  $+1$  parity at the  $\Gamma$  point, but the opposite parity at the  $M$  point as marked in insets.

Ideally, this characterization process needs to be repeated for all bands below the band gaps. This is a complicated task due to the existence of the numerous dispersion curves (see Fig. 1e, f), which result from the multi degrees-of-freedom and coupling between the bolt and the plate. To simplify this, we approximate the system into a lumped-mass model, in which the bolts are modeled as point masses connected to the plate with transverse springs<sup>35</sup> (see “Methods” and Supplementary Note 1 for more details on this model and its validity). As a result, we can calculate the parity for all the bands below the band gap, and

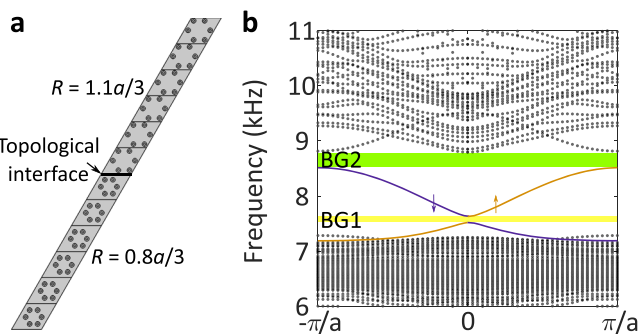


**Fig. 2 Supercell and its dispersion relation.** **a** A supercell made by placing six non-trivial ( $R = 1.1a/3$ ) and six trivial ( $R = 0.8a/3$ ) cells adjacently. **b** Eigenfrequencies of the supercell as a function of wave numbers in the periodic direction. Bulk bands are in black. There are two edge modes with opposite pseudospins (purple and yellow) inside the bulk band gap, where two mini gaps (BG1 and BG2) are generated.

obtain quadrupole 0 and 1/2, and rotation invariants [0, 0] and [2, 0] for the shrunk (trivial) and expanded (nontrivial) unit cells, respectively. This establishes topological distinction of the two band gaps shown in Fig. 1e, f.

**Supercell analysis.** We return to the FEA approach and first perform a supercell analysis by adjoining six non-trivial ( $R = 1.1a/3$ ) and six trivial cells ( $R = 0.8a/3$ ) (Fig. 2a). The terminations are free, and the sides are Floquet-periodic. We observe that the interface hosts chiral propagating modes inside the bulk band gap of the supercell dispersion in Fig. 2b. These propagate in opposite directions with two opposite pseudospins (clockwise and counterclockwise in purple and yellow, respectively), mimicking pseudo spin-Hall effect<sup>36</sup>. However, these edge states are gapped (BG1 and BG2) as opposed to the quantum spin-Hall effect for fermions that supports gapless edge states protected by the time-reversal symmetry<sup>40</sup>. Even though there are ways to close these gaps for a broadband wave propagation at the interface<sup>41</sup>, we deliberately use them to look for potential corner modes in this study. BG1 is the gap in the interface spectrum. This emerges due to the breakage of crystalline  $C_6$  symmetry at the interface and exists as long as there are cells across the interface with different radii  $R$  (see Supplementary Note 2 and Supplementary Fig. 3b). BG2 is at a higher frequency and lies above this interface spectrum and below the bulk spectrum (black). Since BG2 does not exist in the lumped-mass model, in which the bolts are modeled as point masses, we conjecture that BG2 emerges due to the interactions of the finite-sized bolts with the plate.

**Emergence of corner states.** To observe corner states and investigate their differences systematically, we construct a rhombus-shaped, topologically non-trivial domain ( $R = 1.1a/3$ ) inside the trivial domain ( $R = 0.8a/3$ ) (Fig. 3a). This contains two 120° corners and two 60° corners. We also consider the “inverted” configuration, in which the two domains are interchanged. We then perform the eigenfrequency analysis on both the configurations and show the results in Fig. 3b. We observe the emergence of several corner states marked with green and red stars.

In Fig. 3c, we show the low-frequency corner states for the rhombus-shaped structure of Fig. 3a while in Fig. 3d the corner modes of the inverted configuration. These corner states reside in the topological gap BG1. Importantly, we find that only 120° corners support these states. For the verification, we parameterize our system with the unit cells with varying radii and find that these corner states exist robustly even for a small difference in radii between the trivial and non-trivial cells (see Supplementary

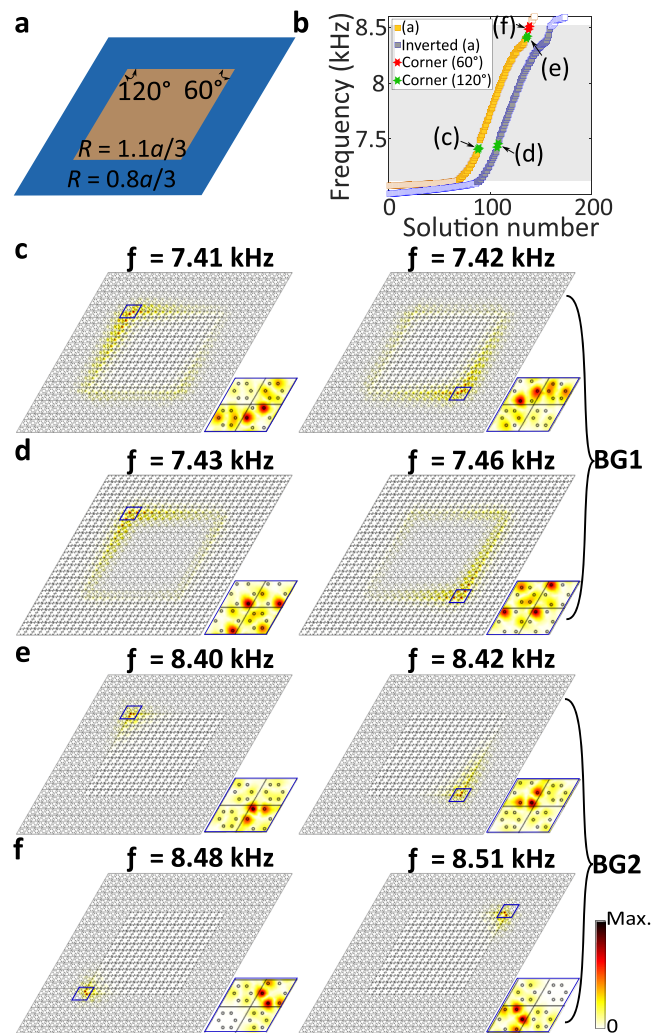


**Fig. 3 The appearance of two kinds of corner state.** **a** A rhombus-shaped structure with an interface between two domains:  $R = 1.1a/3$  (inner) and  $R = 0.8a/3$  (outer). **b** The eigenfrequency for the configuration in (a) and its inverted counterpart. Bulk band gap is marked in gray. Green and red stars represent the corner states. **c-f** Eigenmodes of the corner states corresponding to the stars in (b). The color map represents the amplitude of the out-of-plane displacements,  $|w|$ .

Note 2 for details). Interestingly, there are also high-frequency corner states, marked by red and green stars in Fig. 3b, which reside in BG2. We observe that both 60° and 120° corners support these states as shown in Fig. 3e, f. However, these exist only in the regular configuration shown in Fig. 3a, but not in the inverted configuration. This hints at their nontopological origin, which we again verify by performing a parametric study with varying radii of unit cells (see Supplementary Note 2 and Supplementary Fig. 2 for details). We find that these states exist only for a large difference in radii between the trivial and non-trivial unit cells but are not predicted by our simplified lumped-mass model. This suggests that they appear due to the complex interaction of bolt-plate assembly that the lumped-mass model fails to capture. Their mode shapes also differ from the ones in BG1. For example, the states shown in Fig. 3e have the peak displacement occurring at the most cornered bolt within the non-trivial unit cell, while the adjacent two bolts have nonzero displacements. This is consistent with the topologically-trivial corner modes reported in ref. <sup>32</sup>. Recently, a new type of corner state was discovered due to long-range interactions in a Kagome lattice for electromagnetic

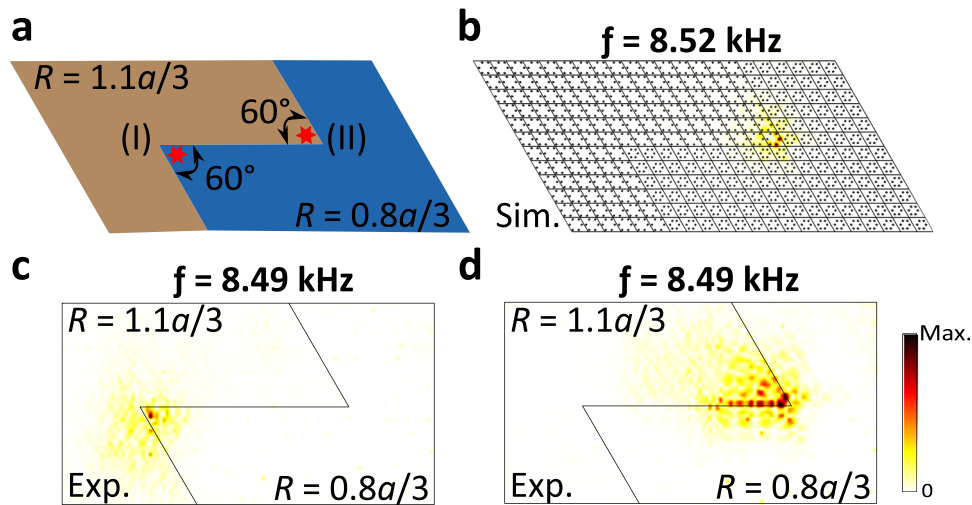


**Fig. 4 Experimental verification of the corner state at 60° corners.** **a** A Z-shaped interface with two different 60° corners is created via placing trivial cells ( $R = 0.8a/3$ ) with non-trivial cells ( $R = 1.1a/3$ ) adjacently. The red stars mark the locations of the piezo-actuators that excite the elastic plate. **b** A simulated eigenmode shows that corner state appear only at the corner (II) at  $f = 8.52$  kHz. **c, d** Experimentally-extracted wave field in the bolted plate when the piezo-actuator is attached on the corner (I) and corner (II), respectively, and excited at  $f = 8.49$  kHz.

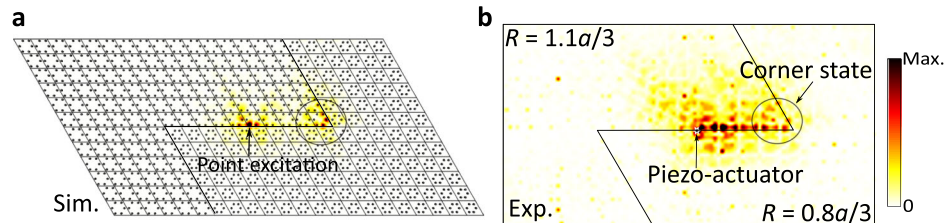


**Fig. 5 Demonstration of asymmetric wave localization when the source excites the middle of the Z-shaped interface.** **a** Simulated wave field with harmonic excitation at  $f = 8.49$  kHz showing the excitation of the corner state on the right. **b** Experimentally-extracted wave field captures the excitation of the corner mode marked within the circle.

waves<sup>42</sup>. Though we study flexural waves in a hexagonal lattice here, it will be an interesting future direction to explore all design parameters in a mechanical system to confirm such a corner state.

What makes the corner states observed in BG2 unique is their tunability when domains are interchanged, and also their novel emergence in this bolted-plate assembly. Moreover, their higher spatial localization helps us realize them in our table-top environment with a smaller sample. These characteristics will be leveraged to achieve one-way energy localization as described below.

**Experimental demonstration.** We build a Z-shaped domain wall that includes two different types of 60° corners in one setup (Fig. 4a, see “Methods” for the fabrication and measurements detail). From the simulation results shown earlier, we know that the corner state in BG2 exists only in the case when the non-trivial cells are surrounded by the trivial cells (Fig. 3e, f), i.e., at corner (II) in Fig. 4a. This is again verified by the eigen-frequency analysis on this particular setup. Figure 4b shows a highly-localized corner state with  $f = 8.52$  kHz at the corner (II).

We excite the plate using a piezoelectric ceramic actuator by placing it at corner (I) and (II) in two separate experiments. We use a chirp signal with the frequency range of 2–40 kHz. A point-by-point measurement is then conducted by using the laser Doppler vibrometer to detect the flexural waves. By gathering and reconstructing measured data from all the points, we plot the steady-state wave-field at  $f = 8.49$  kHz (Fig. 4c, d). When corner (I) is excited, there is no evidence of a corner state apart from the

usual exponentially decaying evanescent field (Fig. 4c). When we excite corner (II), however, we observe clear confinement of energy due to the presence of the corner mode (Fig. 4d). Along with closely matching frequencies, the profile of the corner mode also matches well with the simulation results in that the last two resonators of the non-trivial unit cell have peak displacements (compare Fig. 4b, d). However, there is a slight difference in the profiles obtained numerically and experimentally shown in Fig. 4b, d, respectively. This difference is mainly accentuated along the horizontal interface. We attribute this to the imperfection in the assembly of bolts, by which tiny BG2 could be distorted.

Next, we exploit this selective localization observed in the previous test to demonstrate a one-way localization through the Z-shaped interface. We excite the plate with a harmonic excitation at  $f = 8.49$  kHz in the middle of the interface and show numerical prediction in Fig. 5a. We observe that due to evanescent coupling, it is possible to excite the state at corner (II). At the same time, corner (I) on the left, being at the same distance from the center, does not support any such energy localization as there is no corner mode there. This is verified in the experimental results shown in Fig. 5b. There is a difference in the modal amplitude along the horizontal interface due to the corner mode profile discussed earlier in Fig. 4d. It is however evident that we witness one-way corner localization in our mechanical setup. Such asymmetric wave localization is a highly useful—yet relatively unexplored—feature that can be exploited to manipulate energy flow at will.

**Conclusion.** We propose a ubiquitous design of a bolted plate in the hexagonal arrangement to demonstrate in-gap corner states in our  $C_6$ -symmetry-protected system. By changing the radius of the unit cell, we construct two configurations that show topologically distinct band gaps. We perform topological characterization of the bolted-plate assembly based on a simple lumped-mass model. When two such topologically distinct bolted-plates are placed adjacently, we conduct full geometry simulations to show that there are two regions (mini gaps) in frequency where different types of corner modes can exist. We find that the lower-frequency corner states are of topological origin and the higher-frequency corner states are of nontopological origin. While the former can be predicted by the lumped-mass model, the latter can not. However, the nontopological corner states are highly localized for both  $60^\circ$  and  $120^\circ$  corners and can be made to exist or not based on the inversion of topologically-distinct domains across the interface. This fact is thus used to create a Z-shaped interface between topologically distinct domains for achieving an asymmetric localization of energy. We expect that these findings will enrich the wave-localization phenomena in mechanics and encourage new applications in vibration management.

## Methods

**Numerical modeling of bolted-plate structure.** The commercial finite element software (COMSOL MULTIPHYSICS) is used for numerical modeling. The material properties of the steel bolt are Young's modulus  $E = 210.60$  GPa, density  $\rho = 7800 \text{ kg m}^{-3}$ , and Poisson's ratio  $\nu = 0.30$ . The material properties of the aluminum plate are Young's modulus  $E = 68.9$  GPa, density  $\rho = 2700 \text{ kg m}^{-3}$  and Poisson's ratio  $\nu = 0.33$ . To account for the imperfect mechanical contact between the plate and the bolts, a reduced contact stiffness model can be employed<sup>37</sup>. However, this method is extremely costly in terms of computation time, especially when solving the eigenfrequencies of the full structure. Thus, we employ an alternative, computationally-inexpensive method by altering the bolt's density. The density is determined by computing the frequency of the corner states and match them empirically with those obtained from the measured corner states.

This numerical method based on the finite element method is used not only for the full structure simulations for the corner state calculation, but also for the supercell analysis. In supercell simulation, long sides are set to be periodic boundaries via Floquet periodicity. The short sides of the supercell are set to be free. The boundaries of the rest of finite-element simulations we have conducted are set to be free boundaries.

**Lumped-mass model.** Essential features of the bolted-plate structure can be captured by a simplified lumped-mass model. Let us have points of mass  $m$  attached to a thin elastic plate of thickness  $h$  with a linear spring of stiffness coefficient  $\beta$ . Here we only consider the out-of-plane motion of the plate and masses. Following ref. <sup>35</sup>, we write the equations of motion at frequency  $\omega$  as

$$D\nabla^4 w(\mathbf{r}) - \omega^2 \rho h w(\mathbf{r}) = -\beta \sum_{\alpha} [w(\mathbf{R}_{\alpha}) - \tilde{w}(\mathbf{R}_{\alpha})] \delta(\mathbf{r} - \mathbf{R}_{\alpha}), \quad (1a)$$

$$-\omega^2 m \tilde{w}(\mathbf{R}_{\alpha}) = \beta [w(\mathbf{R}_{\alpha}) - \tilde{w}(\mathbf{R}_{\alpha})], \quad (1b)$$

where  $D = Eh^3/12(1 - \nu^2)$  is the flexural rigidity of the plate,  $w(\mathbf{r})$  is the transverse displacement of the plate at the generalized coordinate  $\mathbf{r} = (x, y)$ ,  $\tilde{w}(\mathbf{R}_{\alpha})$  is the displacement of the resonators attached at points  $\mathbf{R}_{\alpha}$  on the plate, and  $\delta(\mathbf{r})$  is a delta function in two dimensions.  $\alpha = 1, 2, \dots, 6$  for six resonators within the unit cell. We non-dimensionalize frequency and mass as  $\Omega = \omega a^2 \sqrt{\rho h / D}$  and  $\gamma = m / (\rho A_c h)$ , where  $A_c = \sqrt{3} a^2 / 2$  is the area of the unit cell.

We then use the plane wave expansion method to write plate displacement as a superposition of plane waves for a given Bloch wave vector  $\mathbf{k}$  as

$$w(\mathbf{r}) = \sum_{\mathbf{g}} W(\mathbf{g}) e^{-i(\mathbf{k} + \mathbf{g}) \cdot \mathbf{r}}, \quad (2)$$

where  $W(\mathbf{g})$  is the plane wave coefficient as a function of reciprocal lattice vector  $\mathbf{g}$ . Substituting this into the equations of motion, we obtain an eigenvalue problem for  $W(\mathbf{g})$ , which is used to plot the dispersion curve  $\Omega(\mathbf{k})$  (see Supplementary Fig. 1). For detecting the corner states in the rhombus-shaped interface, we treat the whole 2D structure as a unit cell and apply Floquet boundary conditions. We evaluate the solutions at Bloch wave vector  $k = 0$ , which is sufficient to capture the corner states in the system (Supplementary Fig. 3).

**Topological characterization.** We first follow the method based on quadrupole calculated from bulk polarization<sup>38</sup>. The bulk polarization is given as  $P^n = (P_i^n, P_j^n)$ , where  $P_{i,j}^n$  are bulk polarization in two independent directions for the  $n$ th band. For  $C_6$ -symmetric crystalline system as ours, we can calculate the

bulk polarization of a band using the following relation directly<sup>38</sup>:

$$P_i^n = \frac{1}{2} (q_i^n \text{ modulo } 2), \quad (-1)^{q_i^n} = \frac{\eta_n(M_i)}{\eta_n(\Gamma)}, \quad (3)$$

where  $i$  indicates the polarization direction of  $b_i$  (Fig. 1a) and  $\eta_n()$  (parity) denotes the eigenvalue of  $\pi$  rotation over the  $z$  axis for the  $n$ th band.  $M_i$  and  $\Gamma$  are the symmetrical points in the first Brillouin zone.  $q_i^n$  takes odd (even) values when  $\eta_n()$  are opposite (identical) at the  $M_i$  and  $\Gamma$  points. A quadrupole is then defined as<sup>38</sup>

$$Q_{ij} = \sum_{n=1}^N P_i^n P_j^n, \quad (4)$$

where there are  $N$  bands below the band gap. Note that due to  $C_6$  symmetry, we have  $P_i^n = P_j^n$ . See Supplementary Note 1 for the calculations.

Alternatively, we calculate the topological invariant for  $C_6$ -symmetry-protected system as defined in refs. <sup>18,32</sup>. Following the terminology of these papers, bulk topology of our system is classified by:

$$\chi^{(6)} = ([\mathbb{M}], [\mathbb{K}]), \quad (5)$$

where  $[\mathbb{M}], [\mathbb{K}] \in \mathbb{Z}$  are  $C_2$  and  $C_3$  invariants, respectively, and are defined as

$$[\mathbb{M}] = \#M_1 - \#\Gamma_1^{(2)}, \quad (6a)$$

$$[\mathbb{K}] = \#K_1 - \#\Gamma_1^{(3)}, \quad (6b)$$

where  $\#M_1$  ( $\#\Gamma_1^{(2)}$ ) is the number of bands below the band gap with  $C_2$  ( $\pi$ ) rotation eigenvalue  $+1$  at the  $M$  ( $\Gamma$ ) points of the Brillouin zone, and  $\#K_1$  ( $\#\Gamma_1^{(3)}$ ) is the number of bands below the band gap with  $C_3$  ( $\pi/3$ ) rotation eigenvalue  $+1$  at the  $K$  ( $\Gamma$ ) points of the Brillouin zone. See Supplementary Note 1 for the calculations.

**Sample fabrications and experimental measurements.** The plate is  $914 \times 610 \times 2$  mm made of 6061-T6 aluminum and M4-0.7-mm black-oxide alloy steel bolts (91290A180, McMaster-Carr) are chosen as the local resonators. The CNC mill machine is used to drill 1320 through holes and then tap the threads for each hole. Next step is to assemble 1320 steel bolts by using an electric screwdriver with the same torque to fasten those on top of the thin plate. We particularly choose the partially unthreaded bolts so that the unthreaded part is treated as a limiter. A drop of superglue is applied to facilitate the connection between the unthreaded part of steel bolts and thin plate. The fabricated bolted plate can be seen in Supplementary Fig. 4.

The piezo-actuators (STEMiNC, diameter 10 mm, and thickness 1 mm) are bonded on the left corner, middle, and right corner of the bolted plate with silver epoxy adhesive. The input signal of the piezo-actuator is controlled by the function generator and amplified by the voltage amplifier. To perform the measurement, we use the laser Doppler vibrometer mounted on a bi-axial linear moving stage to conduct a point-by-point measurement on the bolted plate with a  $7.5 \times 7.5$  mm square grid. The measurement points are 6600 points in total including 110 points horizontally and 60 points vertically. The piezo-actuator is excited with a chirp signal from 2 to 40 kHz in 100 ms duration. All the measurements are synchronized with the onset input signal from the function generator. After obtaining the data from all of measured points, the fast Fourier transformation is employed to all measured time history profile to get frequency spectrum, which can construct a 2D steady-state transmission map in the frequency of interest. To enhance the visualization of 2D wave field, the cubic interpolation is applied among the measured points.

## Data availability

The data that support plots and related findings of this work are available from the corresponding author upon reasonable request.

## Code availability

The code for obtaining the corner states of this work are available from the corresponding author upon reasonable request.

Received: 12 December 2020; Accepted: 25 May 2021;

Published online: 11 June 2021

## References

1. Nash, L. M. et al. Topological mechanics of gyroscopic metamaterials. *Proc. Natl Acad. Sci.* **112**, 14495–14500 (2015).
2. Wang, P., Lu, L. & Bertoldi, K. Topological phononic crystals with one-way elastic edge waves. *Phys. Rev. Lett.* **115**, 104302 (2015).
3. Mousavi, S. H., Khanikaev, A. B. & Wang, Z. Topologically protected elastic waves in phononic metamaterials. *Nat. Commun.* **6**, 8682 (2015).
4. He, C. et al. Acoustic topological insulator and robust one-way sound transport. *Nat. Phys.* **12**, 1124 (2016).

5. Lu, J. et al. Observation of topological valley transport of sound in sonic crystals. *Nat. Phys.* **13**, 369–374 (2017).
6. Pal, R. K. & Ruzzene, M. Edge waves in plates with resonators: an elastic analogue of the quantum valley hall effect. *New J. Phys.* **19**, 025001 (2017).
7. Liu, T.-W. & Semperlotti, F. Tunable acoustic valley-hall edge states in reconfigurable phononic elastic waveguides. *Phys. Rev. Appl.* **9**, 014001 (2018).
8. Qian, K., Apigo, D. J., Prodan, C., Barlas, Y. & Prodan, E. Topology of the valley-chern effect. *Phys. Rev. B* **98**, 155138 (2018).
9. Ma, J., Sun, K. & Gonella, S. Valley hall in-plane edge states as building blocks for elastodynamic logic circuits. *Phys. Rev. Appl.* **12**, 044015 (2019).
10. Benalcazar, W. A., Bernevig, B. A. & Hughes, T. L. Quantized electric multipole insulators. *Science* **357**, 61–66 (2017).
11. Benalcazar, W. A., Bernevig, B. A. & Hughes, T. L. Electric multipole moments, topological multipole moment pumping, and chiral hinge states in crystalline insulators. *Phys. Rev. B* **96**, 245115 (2017).
12. Schindler, F. et al. Higher-order topological insulators. *Sci. Adv.* **4**, eaat0346 (2018).
13. Serra-Garcia, M. et al. Observation of a phononic quadrupole topological insulator. *Nature* **555**, 342 (2018).
14. Peterson, C. W., Benalcazar, W. A., Hughes, T. L. & Bahl, G. A quantized microwave quadrupole insulator with topologically protected corner states. *Nature* **555**, 346 (2018).
15. Imhof, S. et al. Topoelectrical-circuit realization of topological corner modes. *Nat. Phys.* **14**, 925 (2018).
16. Mittal, S. et al. Photonic quadrupole topological phases. *Nat. Photon.* **13**, 692 (2019).
17. Qi, Y. et al. Acoustic realization of quadrupole topological insulators. *Phys. Rev. Lett.* **124**, 206601 (2020).
18. Benalcazar, W. A., Li, T. & Hughes, T. L. Quantization of fractional corner charge in  $c_n$ -symmetric higher-order topological crystalline insulators. *Phys. Rev. B* **99**, 245151 (2019).
19. Xie, B.-Y. et al. Second-order photonic topological insulator with corner states. *Phys. Rev. B* **98**, 205147 (2018).
20. Chen, X.-D. et al. Direct observation of corner states in second-order topological photonic crystal slabs. *Phys. Rev. Lett.* **122**, 233902 (2019).
21. Chen, Z.-G., Xu, C., Al Jahdali, R., Mei, J. & Wu, Y. Corner states in a second-order acoustic topological insulator as bound states in the continuum. *Phys. Rev. B* **100**, 075120 (2019).
22. Zhang, Z. et al. Deep-subwavelength holey acoustic second-order topological insulators. *Adv. Mater.* **31**, 1904682 (2019).
23. Zhang, X. et al. Second-order topology and multidimensional topological transitions in sonic crystals. *Nat. Phys.* **15**, 582–588 (2019).
24. Zhang, Z., López, M. R., Cheng, Y., Liu, X. & Christensen, J. Non-hermitian sonic second-order topological insulator. *Phys. Rev. Lett.* **122**, 195501 (2019).
25. López, M. R., Zhang, Z., Torrent, D. & Christensen, J. Multiple scattering theory of non-hermitian sonic second-order topological insulators. *Commun. Phys.* **2**, 1–7 (2019).
26. Coutant, A., Achilleos, V., Richoux, O., Theocharis, G. & Pagneux, V. Robustness of topological corner modes against disorder with application to acoustic networks. *Phys. Rev. B* **102**, 214204 (2020).
27. Xue, H., Yang, Y., Gao, F., Chong, Y. & Zhang, B. Acoustic higher-order topological insulator on a kagome lattice. *Nat. Mater.* **18**, 108 (2019).
28. Ni, X., Weiner, M., Alù, A. & Khanikaev, A. B. Observation of higher-order topological acoustic states protected by generalized chiral symmetry. *Nat. Mater.* **18**, 113 (2019).
29. El Hassan, A. et al. Corner states of light in photonic waveguides. *Nat. Photon.* **13**, 697–700 (2019).
30. Chen, Y., Lu, X. & Chen, H. Effect of truncation on photonic corner states in a kagome lattice. *Opt. Lett.* **44**, 4251–4254 (2019).
31. Kempkes, S. et al. Robust zero-energy modes in an electronic higher-order topological insulator. *Nat. Mater.* **18**, 1292–1297 (2019).
32. Noh, J. et al. Topological protection of photonic mid-gap defect modes. *Nat. Photon.* **12**, 408–415 (2018).
33. Xie, B. et al. Higher-order quantum spin hall effect in a photonic crystal. *Nat. Commun.* **11**, 1–8 (2020).
34. Fan, H., Xia, B., Tong, L., Zheng, S. & Yu, D. Elastic higher-order topological insulator with topologically protected corner states. *Phys. Rev. Lett.* **122**, 204301 (2019).
35. Torrent, D., Mayou, D. & Sánchez-Dehesa, J. Elastic analog of graphene: Dirac cones and edge states for flexural waves in thin plates. *Phys. Rev. B* **87**, 115143 (2013).
36. Wu, L.-H. & Hu, X. Scheme for achieving a topological photonic crystal by using dielectric material. *Phys. Rev. Lett.* **114**, 223901 (2015).
37. Chaunsali, R., Chen, C.-W. & Yang, J. Experimental demonstration of topological waveguiding in elastic plates with local resonators. *New J. Phys.* **20**, 113036 (2018).
38. Liu, F., Deng, H.-Y. & Wakabayashi, K. Helical topological edge states in a quadrupole phase. *Phys. Rev. Lett.* **122**, 086804 (2019).
39. Kruthoff, J., de Boer, J., van Wezel, J., Kane, C. L. & Slager, R.-J. Topological classification of crystalline insulators through band structure combinatorics. *Phys. Rev. X* **7**, 041069 (2017).
40. Kane, C. L. & Mele, E. J. Quantum spin hall effect in graphene. *Phys. Rev. Lett.* **95**, 226801 (2005).
41. Liu, T.-W. & Semperlotti, F. Synthetic Kramers pair in phononic elastic plates and helical edge states on a dislocation interface. *Adv. Mater.* **33**, 2005160 (2021).
42. Li, M. et al. Higher-order topological states in photonic kagome crystals with long-range interactions. *Nat. Photon.* **14**, 89–94 (2020).

## Acknowledgements

C.-W.C. and J.Y. are grateful for the support from NSF (CAREER1553202 and EFRI-1741685). R.C. and G.T. acknowledge support by the project CS.MICRO funded under the program Etoiles Montantes of the Region Pays de la Loire. J.C. acknowledges the support from the European Research Council (ERC) through the Starting Grant 714577 PHONO-META and from the MINECO through a Ramón y Cajal grant (Grant No. RYC-2015-17156).

## Author contributions

C.-W.C. and J.Y. conceived the project. C.-W.C. and R.C. conducted and carried out the numerical simulations. C.-W.C. performed the experiment and analyzed the data. C.-W.C. and R.C. prepared the manuscript. All authors extensively contributed to the work and finalizing the manuscript. J.C., G.T., and J.Y. supervised the project. C.-W.C. and R.C. contributed equally to this work.

## Competing interests

The authors declare no competing interests.

## Additional information

**Supplementary information** The online version contains supplementary material available at <https://doi.org/10.1038/s43246-021-00170-x>.

**Correspondence** and requests for materials should be addressed to J.Y.

**Peer review information** *Communications Materials* thanks the anonymous reviewers for their contribution to the peer review of this work. Primary Handling Editor: Aldo Isidori. Peer reviewer reports are available.

**Reprints and permission information** is available at <http://www.nature.com/reprints>

**Publisher's note** Springer Nature remains neutral with regard to jurisdictional claims in published maps and institutional affiliations.



**Open Access** This article is licensed under a Creative Commons Attribution 4.0 International License, which permits use, sharing, adaptation, distribution and reproduction in any medium or format, as long as you give appropriate credit to the original author(s) and the source, provide a link to the Creative Commons license, and indicate if changes were made. The images or other third party material in this article are included in the article's Creative Commons license, unless indicated otherwise in a credit line to the material. If material is not included in the article's Creative Commons license and your intended use is not permitted by statutory regulation or exceeds the permitted use, you will need to obtain permission directly from the copyright holder. To view a copy of this license, visit <http://creativecommons.org/licenses/by/4.0/>.